Measurement of the polarization in large-angle $\pi^- p$ elastic scattering at 2.93 and 3.25 GeV/c

I. P. Auer,* D. Bridges,† T. Droege,‡ D. Hill, R. Giese, R. Miller, K. Nield, P. Rynes, B. Sandler,§ and A. Yokosawa
Argonne National Laboratory, Argonne, Illinois

G. Hicks,‖ D. Miller, and C. Wilson¶
Northwestern University, Evanston, Illinois

(Received 12 March 1981)

We have measured the polarization for elastic scattering in the reaction $\pi^- p \to \pi^- p$ at 2.93 and 3.25 GeV/c using a polarized proton target and multiwire proportional chambers (MWPC's) with emphasis on large-angle scattering. Events were selected by fast scintillation-counter logic. Beam trajectories were measured with four MWPC's and the scattered-particle angles were measured with one or two MWPC's; elastic events were determined by coplanarity and angle-angle correlations. The polarization is in agreement with previous measurements below $|t| = 2.0$ (GeV/c)^2, and crosses from negative to positive near the secondary dip in the differential cross section $d\sigma/dt$. In the backward region, an energy dependence appears with the polarization being large and negative at 2.93 GeV/c and consistent with zero at 3.25 GeV/c.

I. INTRODUCTION

The qualitative features of available differential-cross-section data in both $\pi^- p$ and $\pi^+ p$ backward elastic scattering are represented adequately by baryon-exchange models, $\pi^- p$ backward scattering being described by a pure $I = \frac{3}{2}$ baryon-exchange process, while $\pi^+ p$ scattering has both $I = \frac{1}{2}$ and $I = \frac{3}{2}$ exchanges. None of these models, however are successful at explaining existing $\pi^+ p$ polarization data in the backward region from 1.6 to 6.0 GeV/c.[1] We have measured $\pi^- p$ polarization at 2.93 and 3.25 GeV/c at all angles, concentrating on the backward region. Our limited data in the forward region, where Pomeron exchange is dominant, agree with previous measurements. Our data around 90° center-of-mass scattering angle are consistent with earlier measurements for lower $|t|$, and extend the range to higher values of $|t|$, showing the polarization crossing from negative to positive. Our backward data show an energy-dependent effect that may indicate the presence of a resonance, since similar energy-dependent effects occur near the $N^*(2100)$ and $N^*(2650)$ resonance.

The experiment, which was performed at the Argonne Zero Gradient Synchrotron (ZGS), was the first of a series of experiments designed to make use of multiwire proportional chambers (MWPC's) for measuring the beam and scattered particles. We obtained good spatial resolution and phase-space plots of the incident beam online. A new superconducting magnet SCM1 and ^{3}He-cooled cryostat PPT-III were utilized to obtain a polarized proton target with polarizations of 90%.

Figure 1 is a plan view (not to scale) of the apparatus comprising a two-arm spectrometer. There are four small MWPC's to measure the incident-pion trajectory, but they are not used in

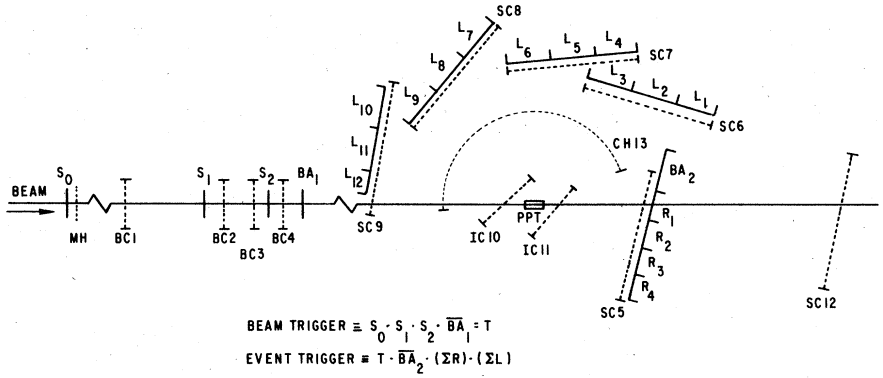

FIG. 1. Plan view of apparatus: S scintillator, MH momentum hodoscope, SC scattering chamber, IC inner chamber, BA beam anticoincidence counter, L left scintillation hodoscope, R right scintillation hodoscope, and PPT polarized proton target.

the fast-trigger logic system. A coincidence of S_0, S_1, and S_2 with the absence of BA_1 (a hole counter) defines a beam particle. Likewise, the scintillation-counter hodoscopes R_1–R_4 and L_1–L_{12} define the presence of scattered particles, while BA_2 vetoes the noninteracting beam particles. Four additional anticoincidence counters, two above and two below the cryostat, are used to veto inelastic processes.

Section II describes the fast-logic system, while Sec. III describes the MWPC's in further detail. Section IV discusses the advantages of the beam MWPC's in obtaining phase-space plots to tune the beam, and Sec. V discusses the use of the scattering MWPC's for locating the target and finding $\pi^- p$ elastic scattering from free protons during the initial tune-up phase of the experiment. Section VI covers the details of reducing the data to obtain the polarization values, and Sec. VII discusses the polarized proton target.

This paper concentrates primarily on the experimental method used in collecting the data, and on the analyses used to obtain the polarization values. Our results are discussed briefly in Sec. VIII.

II. FAST LOGIC

The fast-logic system was set up to reject as much background as possible by using veto counters and by triggering on scintillation-counter coincidences that were timed relative to the beam telescope to within about 10 ns. The trigger requirement is basically the combination of a particle in the beam, none of the veto counters hit, one or more hits on beam right and one or more hits on beam left that are not in veto. This reduces the 5×10^5 π^-/spill down to $\leq$200 triggers/spill, which is about all the computer could accept.

Several different fast-logic triggers were used during the experiment, depending on the range in momentum transfer of interest. The basic components of the system are shown in Fig. 1. Counters S_0, S_1, and S_2 are scintillation counters that form a beam telescope; their areas were $2\times4\times0.125$, $2.5\times2.5\times0.125$, and $2\times2\times0.125$ in., respectively. The anticoincidence counter BA_1 was $4\times4\times0.25$ in. with a 1.25×1.25-in. hole in its center. The coincidence of S_0, S_1, and S_2 with the absence of BA_1 essentially defines the number of particles hitting the target. The R and L counters, as well as the veto counter BA_2, are either 4 or 7 in. wide, 10 in. long, and 0.125 in. thick. The R counters are placed behind the right MWPC with no overlap between them. Counter BA_2 is next to the leftmost R counter, and vetoes the beam. The L counters are placed behind the left-side chambers, and some overlap may occur because the chambers themselves may overlap. Counter L_1 was close enough to the beam that it was normally used to veto the beam as well. A slightly more elaborate trigger allowed some of the R counters to be combined with logical OR's into a right-side veto (RSV) circuit and some of the L counters to similarly form a left-side veto (LSV) circuit. The RSV and LSV were then veto inputs to T. The flexibility of this circuit easily allows selection of the kinematic region of interest.

Additional pole anticoincidence counters A_1 through A_4, which covered the magnet pole face regions to reject inelastic events, consisted of three layers of scintillator each 0.094 in. thick. The first and second layers, closest to the target, were separated by 0.070 in. of tantalum; the second and third layers were separated by 0.120 in. of tantalum, for a total of about 1.2 radiation lengths. The anticoincidence counters also included a threshold Čerenkov counter upstream of the momentum slit to veto electrons contaminating the beam. All of these were combined so that any anticoincidence counter in the chain would veto the event at the master coincidence T. The logic was spill gated, and event gated.

III. MULTIWIRE PROPORTIONAL CHAMBERS AND COMPUTER READOUT

Three different kinds of MWPC's were used during the experiment, all had 2-mm wire spacing. The wires, which were 0.8-mil gold-plated tungsten at a tension of approximately 70 g, were at ground potential. A gas mixture of 70% argon and 30% CO_2 slowly flowed through the chambers. It is common to use argon in combination with an organic quenching agent.[2] Because carbon dioxide does not polymerize under the influence of avalanches, it was chosen in order to keep the chambers clean during the long running periods.

The planar chambers had both X- and Y-measuring wires, while the cylindrical chamber had only angular-measuring wires. The four beam chambers (BC's) had 64 wires in each plane, while the scattering chambers (SC's) had 128 horizontal and 256 vertical wires. The inner chambers (IC's) had 24 horizontal and 128 vertical wires, while the cylindrical chamber (CC) had 512 vertical wires at a radius of 36 cm.

The beam and scattering chambers had their readout electronics mounted on the chamber, with the high-voltage planes located 0.25 in. from the wires. The high-voltage planes were 3-mil aluminized mylar at 4200 V. The cylindrical chamber

had remote readout electronics with 5-mil aluminum high-voltage planes at 4200 V located 0.25 in. from the wires. The inner chambers had remote readout electronics with 3-mil aluminized mylar high-voltage planes at 2800 V located 0.125 in. from the wires. An additional amplifier with a gain of six was added to each cable connecting these wires to the amplifier boards, enabling the threshold to be raised from the usual 1 mV for the other chambers to 5 mV.

The amplifier cards contain eight amplifiers each, producing a fast OR output for each wire hit and a latch that is conditionally set by the fast-logic "store-data" pulse. When the fast electronics-trigger system selects a candidate event, the store-data pulse is sent to latch the hit wires, and the spill gate is closed to turn off the fast electronics to prevent additional beam particles from incrementing event monitor scalars during the time the event is being read into the computer (approximately 1.2 ms) for storage on magnetic tape.

Each event is read into the EMR-6050 on-line computer through an interface that appears to the computer very much like a read-only magnetic tape. The logic control unit begins a scan of all the devices connected to it until it reaches the end of data or until the number of words to be transferred has been reached. Each device can run at its own speed. There are two kinds of events, physics events triggered by the fast logic, and "special data" events triggered by a pulse sent from the computer itself once per ZGS cycle.

The physics events scan a set of six registers first that contain 72 bits of a fixed pattern and 72 bits indicating the status of scintillation-counter tags, such as the momentum hodoscope and right- and left-side trigger counters. Next there are four 24-bit words for the time-to-digital counters that were used during setup. Next the logic control unit reads out the MWPC data through a separate controller that scans the chambers. The planes can be connected to the MWPC bus in any order. The MWPC controller scans each card, skipping empty cards and transferring the hit cards (all eight wires), along with the card number and some control bits, onto the 24-bit LeCroy data bus [Fig. 2(a)].

The "special data" events appear as a set of four 24-bit registers containing 72 bits of a fixed pattern, eight bits free for tags, and 16 bits of polarization data sent from the PDP-11/20 computer monitoring the target. Two words from a digital voltmeter multiplexer are next. The multiplexer advances once each ZGS cycle, and reads in the master high-voltage supplies and beam-line magnet shunts for monitoring. The next 20 words contain the current values displayed on a set of 20 visual scalers. Figure 3(a) schematically indicates the flow of data into the computer.

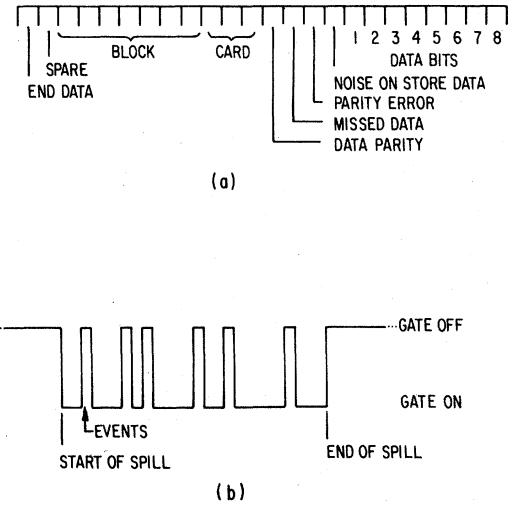

FIG. 2. (a) MWPC data format on LeCroy data bus. (b) ZGS spill-gate structure.

IV. BEAM TUNING

The coordinate system is defined with $X = Y = Z = 0$ at the target center, with Z along the direction of the incident beam, Y up, and X left from beam. Figure 4 shows the beam line. The calculations indicated $\Delta p/p = \pm 2\%$ at the polarized proton target (PPT) located 125 feet downstream from the $0.375 \times 0.375 \times 4$-in. copper target. The calculated beam spot was 0.75 in. in X and 0.5 in. in Y, with a divergence of ± 7 mrad in X and ± 15 mrad in Y.

The first step was to use calculated initial values for magnet settings at a given momentum, and to center the beam in X at the momentum collimator X22MC1 by using the momentum hodoscope positioned just upstream of the collimator. This hodoscope consisted of eight 0.25×1-in. scintillator elements spaced across the beam, and the information was tagged for each event. Bending magnet X22B2 was set to bring the beam into the Wedge magnet X22B3, which in turn brought the beam into four MWPC's, two elements of the telescope, S_1 and S_2, the anticoincidence counter, BA_1, and the PPT.

The advantage of having MWPC's in the beam line is that they provide the ability to tune the beam based on phase-space plots generated on-line. By triggering on the beam telescope, or on one of these counters (S_0), phase-space plots could be displayed on an oscilloscope within a few ZGS cycles. These plots (X vs Y, X vs DX/DZ, and Y vs DY/DZ) cut down the beam tuning time and

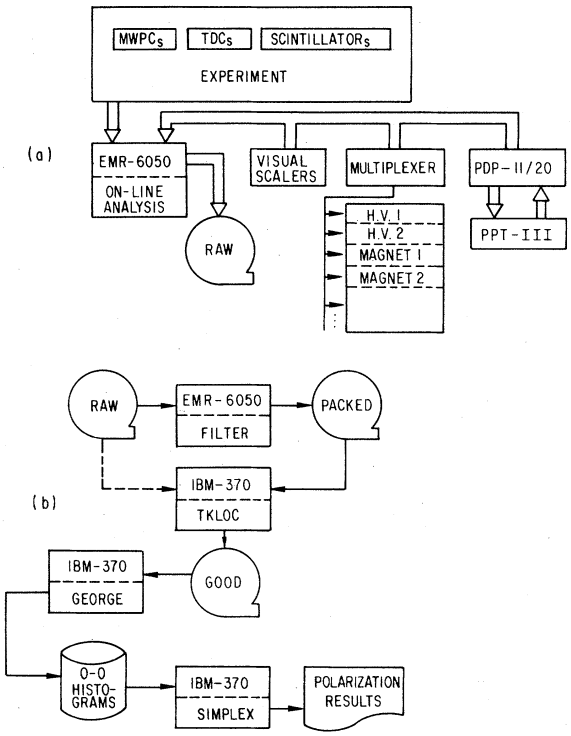

FIG. 3. (a) Schematic representation of hardware interface to collect and record data. (b) Schematic representation of software data reduction of raw data tapes to obtain polarization.

eliminated the need for an x ray of the PPT cryostat to locate the target position.

V. TARGET LOCATION AND ELASTIC FREE PEAKS

The cross section for elastic $\pi^- p$ scattering at low $|t|$ is about 30 mb at 3.0 GeV/c,[3] so initially we put a small $1\times1\times0.125$-in. scintillation counter in the coincidence circuit on the right side of the beam to look for the expected free-proton elastic-scattering peak in the wire map on the left side MWPC. When this was clearly seen, the counter was replaced by a software wire cut that could be applied to both left-side and right-side MWPC's. The cut defines an area within which one or more wires must be seen in X and Y. Any wires seen outside this area veto the event.

The beam is adjusted to be centered at $X=Y=0$ at the target, and is approximately 4×4 cm in size. Those events passing this cut are saved on magnetic tape. When the tape is analyzed and phase-space plots made, we find the defined beam spot to be approximately the target size and to be centered in X and Y, indicating that these events are from a properly aligned target.

VI. DATA HANDLING

All of the programs and subroutines for the on-line EMR-6050 computer were written in assembly

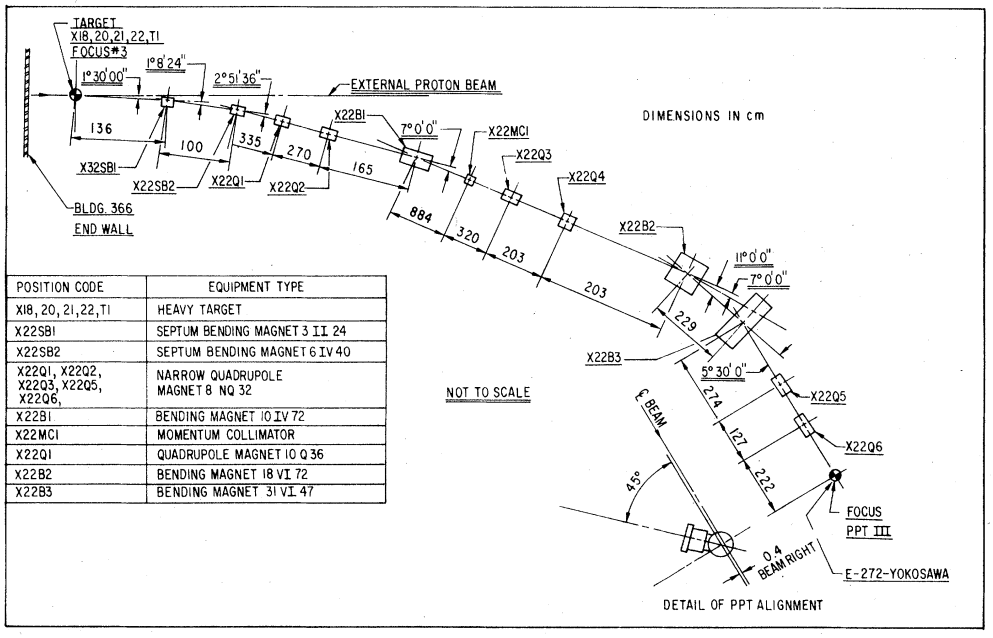

POSITION CODE	EQUIPMENT TYPE
X18, 20, 21, 22, T1	HEAVY TARGET
X22SB1	SEPTUM BENDING MAGNET 3 II 24
X22SB2	SEPTUM BENDING MAGNET 6 IV 40
X22Q1, X22Q2, X22Q3, X22Q5, X22Q6,	NARROW QUADRUPOLE MAGNET 8 NQ 32
X22B1	BENDING MAGNET 10 IV 72
X22MC1	MOMENTUM COLLIMATOR
X22Q1	QUADRUPOLE MAGNET 10 Q 36
X22B2	BENDING MAGNET 18 VI 72
X22B3	BENDING MAGNET 31 VI 47

FIG. 4. ZGS beam line 22B.

language, ASIST. We had a computer unit (CPU) with 32×10^3 24-bit words of core memory, two tape drives, card reader, paper-tape reader/punch, teletype, oscilloscope, line printer, and an interface connected to a LeCroy data bus and controller.

The ZGS had a beam-extraction period (flat top) of approximately 0.6 s, and a total acceleration cycle of approximately 4 s. Typical beam intensities were 50×10^5 π^-/spill. At the beginning of each spill, the spill gate is opened [see Fig. 2(b)] to enable the fast electronics to detect events and monitor associated counting rates. Event analysis is not allowed during the beam spill. When the fast-logic triggers, the spill gate is closed and the event is read into a "raw" data buffer in the computer memory. Concurrently with this, and between events, events in the raw data buffer are validated, compressed, and placed in a "packed" buffer that holds about 35 events. When the event read-in is complete, the spill gate is turned on only if there is room for another event in the raw buffer. When the packed buffer is full, a write operation to magnetic tape is initiated which proceeds concurrently with the above. After the end of the spill a signal is sent to the PDP-11/20 [see Fig. 3(a) and Sec. VII] to obtain the current target polarization and the previously mentioned "special data" event is read in and placed in the packed buffer.

The tapes contain all of the scintillation-counter tags and MWPC data for each event, the target polarization and scaler values, and one of the magnet or power supply's values for each spill. Events are analyzed between spills primarily to obtain diagnostic information that can be displayed on the oscilloscope or printed during the run. For beam tuning, tracks are reconstructed for the beam chambers and phase-space plots are available.

Since this was an asymmetry measurement, it was important to maintain running conditions as constant as possible for each set of "matching" runs. A matching set of runs is two or more runs where the number of particles hitting the positively polarized target equals the number of particles hitting the negatively polarized target. The target polarization was reversed at three-hour intervals, typically.

Since the polarization of the target was reversed by changing the frequency of the microwave power supplied to it, we did not need to have a symmetric apparatus nor know the detection efficiency of the equipment as long as it remained constant for the matching set of runs.

Monitoring of the beam and equipment on a run-by-run basis was necessary to ensure that the data could be grouped into matching sets. The more important monitors at our disposal were in the form of ratios. Dead time was determined from the number of particles in the gated-beam telescope divided by the ungated-beam telescope count. We also measured the beam accidental rate, the number of triggers per particle in the telescope, the number of particles per spill, and the rates of all the scintillation counters that were not in veto. The fact that the ratio of particles hitting the target, T^+/T^-, was close to the ratio of the noncoplanar background determined later in the analysis, $\mathrm{NCP}^+/\mathrm{NCP}^-$, shows that the runs did match.

The cylindrical chamber was used only in the last series of runs, and was useful for rejecting background events.

A. Filtering

The data were filtered on the EMR-6050 computer, with the program FILTER, and cuts were made to remove events that triggered but had problems that would preclude their reconstruction. Some of the data were filtered on the IBM-370/195 computer, with the program TKLOC, which had the capabilities of FILTER but additionally computed the beam trajectories $Y=aZ+b$ and $X=a'Z+b'$, and wrote an output tape of only good events in a FORTRAN-usable form. The output of FILTER was also processed by TKLOC to compute the beam trajectories and reformat the data. Figure 3 schematically indicates the flow of data from the experimental apparatus onto the raw data tapes, and the software procedures that reduced these tapes to obtain the polarization values.

The first requirement in the filter was to guarantee that only one particle scattered to beam right and one to beam left by looking at the R and L counters. Only one (or two adjacent) R counters and one (or two adjacent) L counters were allowed.

The next requirement was to make a fast kinematic check from the trigger counters. A kinematics program was written that generated events at the target center and calculated the trajectories of the π^- and p through the magnetic field to the chambers as discussed below. At 3.25 GeV/c, for example, backward scattering of the π^- requires the proton to scatter within 15° of beam right. A correlation matrix was made that was 4×9 or 4×12 (since there were four R's and either nine or 12 L's). For a given R counter, the matrix defined which L counters were allowed to fire as determined by kinematic constraints.

Since the trigger was based on the scintillation counters, and the MWPC's contained noise and possibly memory of previous events (or the beam),

the MWPC data were cleaned up by removing vertical wires from the data if they were not in the shadow of a trigger counter that fired. The position of the shadows was determined for each counter from the data itself by looking at the wire maps produced when the selected trigger counter (R or L) was hit. Thus 13 or 16 sets of maps were produced, one for each counter.

In general, when a particle passes through a chamber it will generate a hit in more than one wire, depending on the electronics timing, type of gas, angle of incidence, etc. Clusters of wires are considered a single hit if they contain five or fewer wires, and any gaps within the cluster can be no wider than one wire. The barycentric center of the cluster is used for its position in terms of wire number. Some of the chambers overlapped others, so it was possible for a single particle to produce two clusters. Since the beam also went through a chamber, it was possible to have three clusters on the set of beam-left chambers. Similar combinations occurred with the horizontal wires, and the software logic sorted the various combinations and kept only those events that potentially had one scattered particle on each side of the beam.

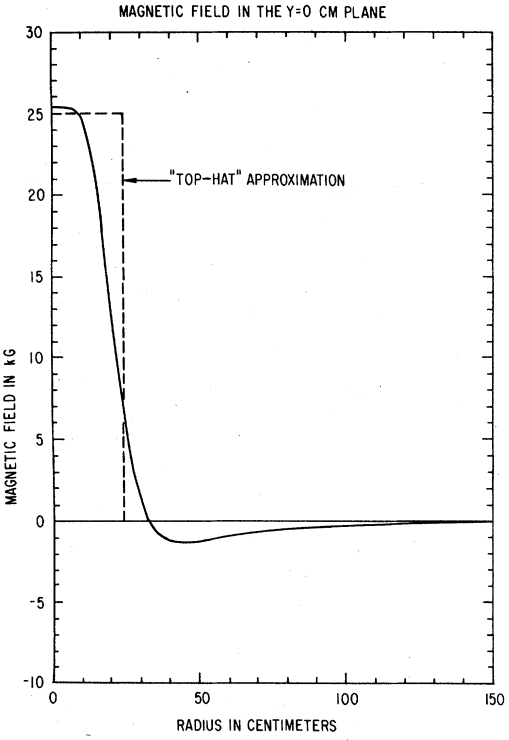

FIG. 5. Magnetic field in the $Y=0$ plane (dashed curve shows the top-hat approximation).

B. Magnetic-field corrections

The superconducting magnet SCM1 is essentially two Helmholtz-coil pairs. A computer calculation gives the field shown in Fig. 5 which has a uniformity of three parts in 10^4 in the central volume of 200 cm^3 of 5-cm radius.

The problem of reconstructing the interaction vertex of a scattering process is greatly simplified if the particles are not bent by the magnetic field of the target magnet. By making a correction to the detected hits in the chambers to find points in space through which the particles would have passed in the absence of the field, we can connect these points by straight lines that are then the trajectories used for event reconstruction.

For a particle moving from the center of a uniform top-hat field to its edge, the angle of bend is given by

$$\theta = 2\sin^{-1}(R/2\rho), \tag{6.1}$$

where $R = 20$ cm is the radius of the field and $\rho = Pc/0.3H$ is the radius of curvature in the field in cm, P is the momentum of the particle in MeV/c, and H is the magnetic field in kG. The beam is assumed to be parallel to the Z axis, and bends in the field to arrive at the vertex $X = Y = Z = 0$. A value is chosen for the angle of the proton in the equatorial plane, and the corresponding angle of the pion is calculated, as well as the energies and momenta, using kinematics for elastic scattering. The target is assumed to have density of 1 gm/cm^3 with dimensions of $2\times2\times8$ cm. The path length in the target is determined for each particle from a straight line at the calculated production angle in order to approximate the momentum loss in the target. The production angles and reduced particle momenta are used, and the angle of bend to reach the field edge is found. The particles then follow straight lines until they hit the chamber of interest. Each trajectory is also projected in a straight line along its production angle until it hits the chamber or an extension of it. The distance between the two positions is saved as a correction value, along with the coordinate of the expected intersection point. This process is repeated for a range of proton scattering angles to cover the chamber. A fourth-order least-squares fit is made of the correction value as a function of the chamber coordinate. For the inner chambers, which lie inside the 20-cm radius, and the cylindrical chamber, the calculations are altered in finding the hit positions, but the scheme is the same. The correction values vary in the scattering chambers from 1.5 cm in chamber 5 to 26 cm in chamber 9 for 3.5 GeV/c. The inner-chamber correction is, at most, 0.22 cm. The cylindrical-chamber correction varies from 2°

to 16°.

The momentum transfer is defined by the particle on beam right, normally the recoil proton, and the magnetic-field correction is fairly good because the energy loss is small. The fast pion need not be corrected for the magnetic field since we are measuring an asymmetry, and results computed without field corrections are found to be consistent with those made with field corrections in the backward region where particle identification is not a problem.

Near the 90° region in the center of mass, the proton can go to beam-right or beam-left and we have no method of particle identification, so these data are analyzed twice. If we choose to define on what we assume is a proton in chamber 5 (beam-right) and look at the conjugate distribution in chamber 6 (beam-left) we expect to see the free peak at the angle given by the kinematics of elastic scattering.

C. Event reconstruction

The input tape for event reconstruction is labeled "good" in Fig. 3(b); it contains all hardware information about each event, as well as its beam trajectory. The program GEORGE reconstructs the polar angle θ and the azimuth ϕ of the two scattered particles in one of three different modes depending on the value of the variable I_Z (0, 1, or 2).

For $I_Z = 0$, only one scattering chamber is used on beam-right and one on beam-left, and the vertex is assumed to be at $Z = 0$. For $I_Z = 1$, only one scattering chamber is used on beam-right, and the beam-left inner chamber plus one left-side scattering chamber are used to determine the Z position where the beam trajectory crosses the straight-line projection between the hits in the two left-side chambers. The case $I_Z = 2$ is similar to $I_Z = 1$, except that the right-side inner chamber and one right-side scattering chamber are used with only one left-side scattering chamber to determine the Z of the vertex.

The output of GEORGE is a set of nine 20×20 scatter plots of θ_R vs θ_L. The width and range of the bins are adjustable to suit the region of interest, forward, 90°, or backward. Three $\Delta\phi$ values are used to produce six of the nine histograms. Normally these values are 6°, 10°, and 15°, and the plots are coplanar or noncoplanar, depending on whether $\Delta\phi$ is less than or greater than the selected value. ($\Delta\phi$ is defined as $\phi_R - \phi_L - 180°$.) The other three scatter plots provide for ranges of $\Delta\phi$, and are normally set at 10°–30°, 15°–30°, and 20°–30° and are used for the background normalization when a sharp cut, for example at the 6° boundary, is not desirable. To choose different values for these variables, GEORGE has to be run again. A scatter plot of θ_R vs $\Delta\phi$ is also output to indicate where to set the limits to differentiate between the elastic scatters and background, noncoplanar, events.

D. Background subtraction

The SIMPLEX program reads the nine histograms and selects one noncoplanar plot and one coplanar plot to be used for a set of positive polarization runs and the corresponding plots for a set of negative polarization runs. Since the noncoplanar background is similar for positive and negative runs, the background is always summed to obtain better statistics. A weighted sum of the bins on each side of the free-peak region is made to find two scale factors η_L and η_R, such that the differences between the coplanar and noncoplanar curves are minimized on the left and right sides, respectively. If all the bins on one side are being ignored, then the scale factor from the other side is used; otherwise the weighted average of η_L and η_R are used to form the factor η. The values of η_L and η_R were typically within 5% of each other. This fact, and the observation that the coplanar and noncoplanar data are similar outside the free-peak region, gives us confidence that the background under the free-proton peak in the coplanar data can be determined by using the noncoplanar data. In addition, scattering from a pure carbon target results in coplanar data with the same shape as the noncoplanar data. The noncoplanar data in each bin are multiplied by η to form a normalized background. The normalized background in the free-peak region is subtracted from the coplanar data in the free-peak region to find the number of elastic scattering events from free protons. These numbers for both values of target polarization are then used to determine the polarization, as described in the next section.

Figure 6 shows a sample distribution for backward elastic scattering when the inner chamber on beam left was used ($I_Z = 1$). The dashed lines delineate the region in which the free peak is expected to appear. The solid circle is used to indicate the magnitude of coplanar data and the open circle indicates the magnitude of the noncoplanar data multiplied by η. In this case, the coplanar data are for $\Delta\phi < 6°$ and the noncoplanar data are for $15° < \Delta\phi < 30°$. The bin width is 1°, with the first bin centered on 0.5°.

E. Polarization calculations

The difference mentioned above can be used to calculate the differential cross section, provided

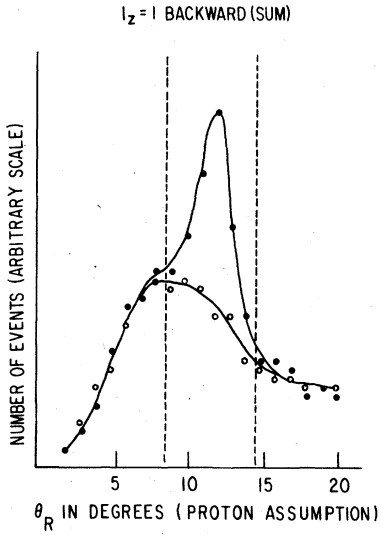

FIG. 6. Sample data from program SIMPLEX indicating the free-peak region for $I_Z=1$. The pion is at 108° on beam-left. This is the conjugate distribution of the proton and the bin width is 1° per bin.

we know the acceptance and efficiencies of the detection equipment, and the beam flux, and provided that the efficiencies remained constant for long periods of running. For polarization measurements we only need to know the differences in the rates of scattering over relatively short sets of runs (several hours), during which the efficiencies could be kept reasonably constant.

The background under the free peak, B, includes both the positive and negative data; it was scaled by the factor η to match the coplanar data in the wings. There we obtained the number of elastic events by

$$N^+ = S^+ - B\eta T^+/(T^+ + T^-),$$
$$N^- = S^- - B\eta T^-/(T^+ + T^-), \tag{6.2}$$

where N^+ and N^- are the true number of free events normalized for equal beam flux, S^+ and S^- are the number of events in the free peak (including background), B is the background, η is the scale factor, and T^+ and T^- are the number of particles hitting the target. The polarization is given by

$$\frac{N^+}{T^+} = \frac{N^0}{T^0}[1 + P(\theta)P_T^+],$$
$$\frac{N^-}{T^-} = \frac{N^0}{T^0}[1 - P(\theta)P_T^-], \tag{6.3}$$

where N^0 is the true number of free events that would have been obtained with T^0 particles incident on an unpolarized target, $P(\theta)$ is the polarization, and $P_T^\pm$ is the target polarization. Solving for $P(\theta)$ gives

$$P(\theta) = \frac{N^+/T^+ - N^-/T^-}{(N^+/T^+)P_T^- + (N^-/T^-)P_T^+}. \tag{6.4}$$

In terms of the ratio $R = T^+/T^-$ we have

$$P(\theta) = \frac{N^+ - RN^-}{N^+P_T^- + RN^-P_T^+}. \tag{6.5}$$

For a matching set of runs, T^+ is approximately equal to T^-. If the noncoplanar background (NCP) contains no elastically scattered events [coplanar (CP)], then the ratio $\mathrm{NCP}^+/\mathrm{NCP}^-$ should be approximately equal to R. The T's have to be normalized for various conditions that preclude the analysis of some events, such as two beam tracks or hardware readout malfunctions. In general, when the equipment is running well, the T^+/T^- ratio is close to the $\mathrm{NCP}^+/\mathrm{NCP}^-$ ratio after the normalization is made, and the T^+/T^- ratio is used. In performing the normalization, some runs appear abnormal (due to equipment failure) and can be skipped before GEORGE is run to prevent any bias.

Including the background subtraction in Eq. (6.5) yields

$$P(\theta) = \frac{S^+ - RS^-}{S^+P_T^- + S^-RP_T^+ - \dfrac{(P_T^+ + P_T^-)B\eta}{(1+1/R)}}. \tag{6.6}$$

The error in this polarization is taken to be statistical, so we take the partial derivatives with respect to each physically independent variable:

$$|\Delta P|^2 = \left|\frac{\partial P}{\partial S^+}\right|^2 |\Delta S^+|^2 + \left|\frac{\partial P}{\partial S^-}\right|^2 |\Delta S^-|^2 + \left|\frac{\partial P}{\partial B}\right|^2 |\Delta B|^2 + \left|\frac{\partial P}{\partial \eta}\right|^2 |\Delta \eta|^2. \tag{6.7}$$

If the data have a Gaussian distribution we have

$$|\Delta S^+|^2 = S^+, \quad |\Delta S^-|^2 = S^-, \quad |\Delta B|^2 = B. \tag{6.8}$$

Since η is evaluated in the wings of the distribution to make the CP and NCP data match, in the first order it is given by $\eta = \mathrm{CP}/\mathrm{NCP}$. The data quoted in the tables do not include a systematic error of approximately 0.04, which is the estimated error in the target polarization.

VII. POLARIZED PROTON TARGET

The polarized proton target (PPT) used was PPT-III, designed and built at ANL. This target has the N-type design, that is, the direction of polarization is normal to the nominal plane of scattering. Specifically, the spin axis is vertical, and scattering is in the horizontal plane. The

aperture of the target magnet allows one to detect events with the normal to the scattering plane at an angle as large as $\pm 30°$ to the vertical.

The magnet used with this target consists of two pairs of superconducting Helmholtz coils. This arrangement provides a field of 2.5 T in a cylindrical volume, 2 cm high, and 5 cm in radius, with field uniformity $\Delta B/B < \pm 0.0003$. The target cryostat is a horizontal continuous-flow ^{3}He refrigerator with ^{4}He precooling. The main ^{3}He pump is of the oil-booster type,[4] which permits operation at a ^{3}He temperature of ~0.4 K with a total target heat load of 25 mW.

The target material was ethylene glycol, doped with potassium dichromate and frozen in the form of ~2-mm-diameter spheres. The target length was 8 cm, and the lateral dimensions were 2 cm each. The density of the target was measured to be $0.82 \pm .05$ g/cm^3. The composition of the target material, by weight, was as follows: C (34%), H (8.3%), O (49%), K (3.9%), Cr (5.1%). The hydrogen nuclei were polarized by microwave dynamic nuclear cooling.[5]

A computer-based nuclear-magnetic-resonance (NMR) spectrometer was developed for on-line measurement of the target polarization. A PDP-11/20 computer was used to extract the NMR signals from the background noise, provide on-line polarization values, and monitor the target for performance optimization.

Figure 7 is a diagram of the NMR spectrometer electronics. The computer first samples the central value of the voltage-controlled oscillator (VCO) using the frequency counter, and determines the range of a linear voltage ramp to frequency-modulate the VCO by ± 200 KHz around a central value of 108 MHz. The voltage range of the digital-to-analog converter was -10 to 10 V, and 256 points were sampled over a range of 18.75 V, so the VCO could drift by ± 13 KHz before problems arose.

After attenuation in a constant-current source, this signal is sent to the parallel-resonance tuned circuit consisting of the NMR target coil, the 30 pF tuning capacitor, and a $\frac{3}{2}$-wavelength-long cable. The presence of the nuclear spins causes the tuned circuit to modulate the amplitude of the signal, which is amplified and sent to a diode detector triplet with high- and low-pass filters. This signal is sent directly to the computer as the V signal. To form the DV signal, a dummy circuit produces a signal of similar amplitude and general shape. This dummy signal is inverted and summed with the NMR signal and a signal proportional to the ramp, so that the characteristic nonlinearities in the electronics can be minimized, and so that the magnitude of the high-frequency noise does not exceed the 10 V limit of the analog-to-digital con-

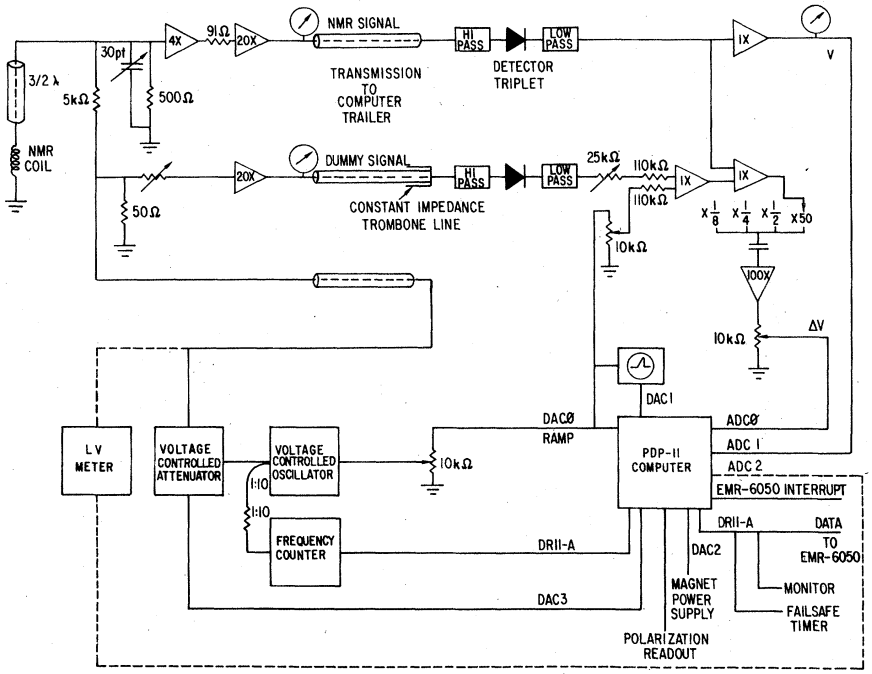

FIG. 7. NMR spectrometer block diagram.

verters. This is important in measuring the "thermal equilibrium" (TE) polarization, where the noise along with the signal is amplified 200 times more than the enhanced polarization signal. A voltage lookup table is used to correct for nonlinearities in the diode triplet.

The NMR data are acquired at a ramp repetition rate of about 100 Hz. To reduce high-frequency noise, 1000 DV-type sweeps are averaged and 100 V-type sweeps are averaged. Low-frequency noise is only a problem in the TE signals, and has a time constant on the order of minutes. This is reduced by measuring the TE signals enough times (typically 100) so that the standard deviation of the mean area under the TE signal is less than one percent.

The background signal (spectrometer response in the absence of nuclear resonance) must be subtracted to obtain the signal area needed to calculate the polarization. The background shape is obtained, approximately once every hour, by shifting the magnetic field by +15 mT for positive enhancement and −15 mT for negative enhancement. A signal is then taken in the usual way and this DV "baseline" is subtracted from all NMR DV signals taken before any processing is done. In the TE case, the magnet is alternately changed by ±15 mT. Second-order corrections to the polarization values are made as in Ref. 6.

The program is written in assembly language for the PDP-11/20 computer and used by many target operators, some of whom are not familiar with computers. The operating system was designed to be small, fast, easy-to-use, and flexible. It appears to the operator as a set of 49 items in a menu of tasks to be executed. Nine of these tasks acquire and analyze target data; the others perform calculations or some utility function. During data acquisition, as a convenience to the operator, a background program can be activated. This background program operates in the same way as the main (or foreground) program, except that it can only execute a nonconflicting subset of the 49 tasks.

During data taking, the program displays the polarization on a numeric LED readout and the NMR signals on an oscilloscope. It controls the magnet power supply to correct for drift and to make the necessary 15 mT shifts for baseline recording. Upon request, the polarization and/or status of the target is transmitted to the main experimental computer.

VIII. DISCUSSION OF RESULTS

Earlier polarization measurements[7-9] in πp elastic scattering up to $|t| \approx 2.0$ (GeV/c)^2 show a mirror symmetry, $P(\pi^+ p) \approx -P(\pi^- p)$, due to the interference of $I=0$ and $I=1$ exchange in the t channel. A secondary dip in the cross section near $|t| = 2.8$ (GeV/c)^2 has made measurements beyond $|t| \approx 2.0$ (GeV/c)^2 difficult. Our measurements investigate this region, which also extends past the center-of-mass angle of 90°, and are shown in Fig. 8 (tabulated in Tables I and II). Figure 9 shows previous measurements for $\pi^+ p$ elastic scattering for comparison. The interesting aspect of our data (also seen in the $\pi^+ p$ data) is the change in sign from negative to positive polarization near this second dip in the cross section.

The classical optical model of absorption and scattering by an opaque disk of radius 1 fm, the range of the strong interaction, describes some of the gross features. The elastic cross section is equal to the inelastic cross section, and represents diffraction scattering. The angular distribution of the elastic scattering is the Fourier transform of the spatial distribution of the target particle and, for the lth partial wave, it is repre-

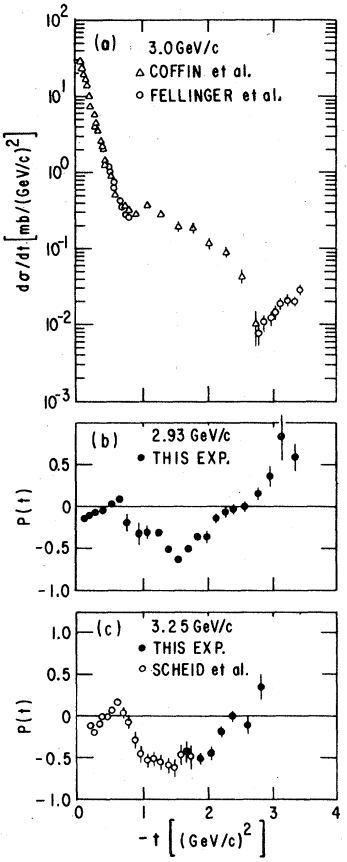

FIG. 8. (a) Differential cross section for $\pi^- p$ elastic scattering at 3.0 GeV/c. (b) Polarization for $\pi^- p$ elastic scattering at 2.93 GeV/c. (c) Polarization for $\pi^- p$ elastic scattering at 3.25 GeV/c.

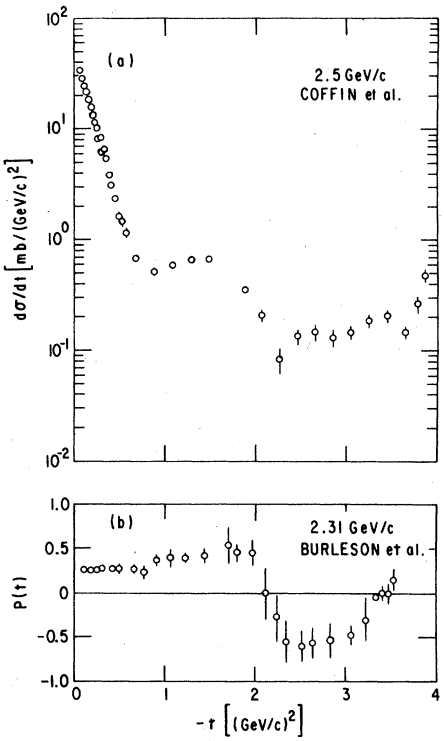

FIG. 9. (a) Differential cross-section for π^+p elastic scattering at 2.5 GeV/c. (b) Polarization for π^+p elastic scattering at 2.31 GeV/c.

sented by $P_l(\cos\theta)$.[10] For small angles, $q^2<0.2$ (GeV/c)^2, the sum over the Legendre polynomials is proportional to a first-order Bessel function. This model, however, does not account for the elastic scattering shape at higher momentum transfer, nor does it give any energy-dependence information.

The strong forward peak can also be described by a peripheral interaction in which many partial waves are involved. In elastic scattering of π^-p we can write the total cross section and polarization in terms of the nonflip, $f(\theta)$, and spin-flip, $g(\theta)$, amplitudes as

$$\sigma = |f|^2 + |g|^2 \tag{8.1}$$

and

$$\sigma P = |fg^*|\,, \tag{8.2}$$

where

$$f(\theta) = \sum_{l=1}^{N} [(l+1)A_{l+1/2} + lA_{l-1/2}]P_l(\cos\theta) \tag{8.3}$$

and

$$g(\theta) = \sum_{l=1}^{N} (A_{l+1/2} - A_{l-1/2})P_l'(\cos\theta)\,, \tag{8.4}$$

TABLE I. Polarization at 2.93 GeV/c for π^-p elastic scattering.

$-t$ [(GeV/c)^2]	P
0.125	−0.134 ± 0.037
0.204	−0.122 ± 0.020
0.298	−0.082 ± 0.018
0.408	−0.066 ± 0.024
0.529	0.035 ± 0.037
0.660	0.082 ± 0.063
0.860	−0.194 ± 0.098
0.045	−0.322 ± 0.122
1.094	−0.312 ± 0.075
1.245	−0.328 ± 0.057
1.397	−0.517 ± 0.044
1.548	−0.630 ± 0.041
1.697	−0.515 ± 0.046
1.843	−0.364 ± 0.053
1.986	−0.363 ± 0.069
2.124	−0.145 ± 0.060
2.258	−0.082 ± 0.084
2.379	−0.048 ± 0.064
2.548	−0.015 ± 0.065
2.747	0.137 ± 0.077
2.936	0.351 ± 0.137
3.128	0.821 ± 0.282
3.321	0.577 ± 0.167
3.865	−0.462 ± 0.123
4.048	−0.354 ± 0.084
4.195	−0.261 ± 0.065
4.314	−0.070 ± 0.058
4.410	−0.050 ± 0.057
4.487	−0.396 ± 0.152
4.550	−0.613 ± 0.112
4.600	−0.693 ± 0.165
4.639	−0.667 ± 0.144
4.670	−0.499 ± 0.088

TABLE II. Polarization at 3.25 GeV/c for π^-p elastic scattering.

$-t$ [(GeV/c)^2]	P
1.67	−0.439 ± 0.139
1.85	−0.521 ± 0.064
2.02	−0.459 ± 0.070
2.19	−0.202 ± 0.060
2.37	−0.010 ± 0.072
2.58	−0.119 ± 0.112
2.78	0.339 ± 0.155
4.418	0.005 ± 0.146
4.610	0.020 ± 0.077
4.765	−0.200 ± 0.108
4.889	−0.046 ± 0.094
4.989	0.004 ± 0.059
5.070	−0.099 ± 0.047
5.134	−0.149 ± 0.109
5.186	−0.073 ± 0.066
5.227	−0.021 ± 0.143
5.258	0.046 ± 0.179

where $J = l \pm \frac{1}{2}$ and $A = (\eta e^{2i\delta} - 1)/2i$, with δ being the phase shift and η being the amplitude of the particular partial wave. For higher values of incident pion momentum (above 2 GeV/c) the partial-wave analysis becomes very difficult, because the number of partial waves required increases with energy, and accurate measurements are needed at all angles.

To describe the scattering amplitude, it is convenient to use the Mandelstam variables in the reaction $A + B \to C + D$ (e.g., $\pi^- p \to \pi^- p$ as in this study):

$$s = (P_A + P_B)^2 ,$$
$$t = (P_C - P_A)^2 , \qquad (8.5)$$
$$u = (P_D - P_A)^2 .$$

The s channel is the direct channel, and formation resonances are observed when the total center-of-momentum system (c.m.s.) energy, $\sqrt{s}$, reaches the energy of the resonance. This mechanism is dominant[10] for small values of s, and the baryon resonances $N_\alpha(1688)$, $N_\gamma(1525)$, and $\Delta_\delta(1236)$ are examples. The exchange of poles in the t channel corresponds to formation resonances in the direct channel. These s-channel resonances are most readily seen in the backward region for $\pi^- p$ elastic scattering where the diffractive effects, or pomeron exchanges, are small. The total cross section, a function of energy in πp scattering, smooths out above 2.5 GeV/c and resonant bumps are not easily observed. (The data in Figs. 8–12 are taken from Refs. 11–23.) The energy dependence of the polarization, however, shows structure which may indicate the presence of new resonances. For example, structure in polarization may be caused by the interference of s-channel resonances and a background term. The background term can be estimated from phase-shift analysis.[13] This approach applied to $\pi^- p$ elastic scattering near 2.0 GeV predicts that the polarization is negative in the u channel (in the range $-0.2 > u > -1.0$ GeV/c) for incident pion momenta just below the s-channel resonance, crosses through zero at the resonance, and then becomes positive above the resonance. This is shown in Fig. 10 for the $N^*(2190)$ at a laboratory momentum of 2.07 GeV/c, and a similar result is shown in Fig. 11 for our data on the $N^*(2650)$ at a laboratory momentum of 3.25 GeV/c. The $N^*(2650)$ has been seen in total cross sections, and is assumed to be a Regge recurrence of the $N^*(2190)$, but perhaps this method can provide information useful in determining its J value.

If the reaction involves a simple exchange in the u channel, and is peripheral, then $\pi^- p$ scattering in the backward region might satisfy a "derivative relationship" between the differential cross section and the polarization[14] of the form

$$P(u) = \delta(\theta)(2q^2 \cos\theta_{cm}) \frac{\partial}{\partial \mu} [\ln\sigma(u)] , \qquad (8.6)$$

where $\sigma(u) = d\sigma/du$ is the differential cross sec-

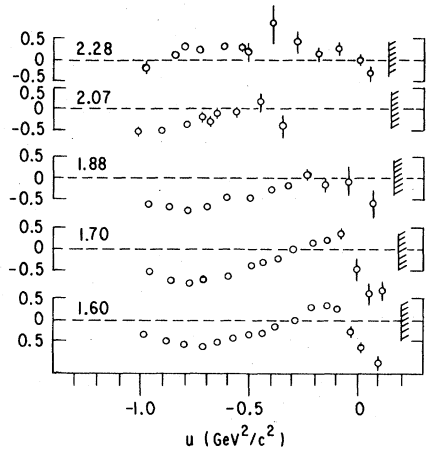

FIG. 10. Polarization for $\pi^- p$ elastic scattering in the backward region as a function of u for incident beam momenta of 1.60, 1.70, 1.88, 2.07, and 2.28 GeV/c (see Ref. 21).

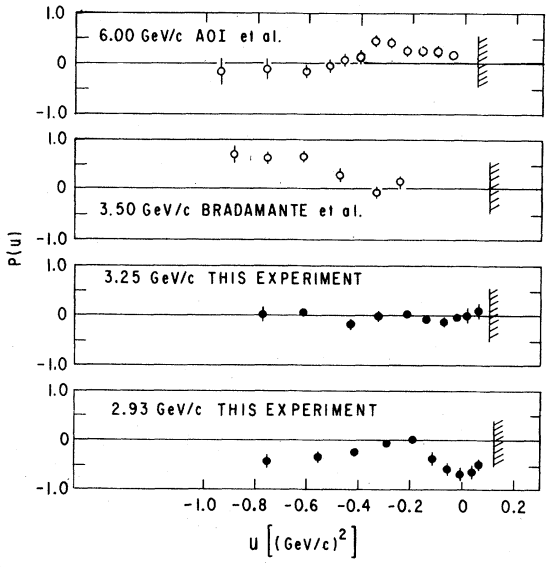

FIG. 11. Polarization for $\pi^- p$ elastic scattering in the backward region as a function of u for incident beam momenta of 2.93, 3.25, 3.50, and 6.00 GeV/c.

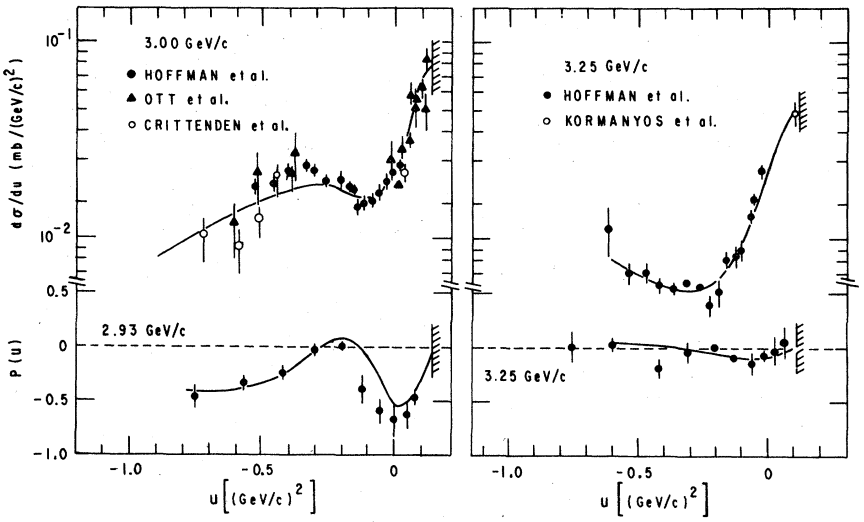

FIG. 12. Differential cross section and polarization as a function of u in the backward direction indicating the success of the "derivative rule" for this experiment.

tion and $\delta(\theta)$ is a scale factor. Figure 12 shows our data in the backward region. The smooth curve through the differential cross section is an eyeball fit to the data for both the 3.0 and 3.25 data. The curves through the polarization data are derived by applying the derivative relationship to these cross-section curves. The relationship is satisfied, suggesting the reaction is indeed peripheral in the backward region.

In addition, an attempt was made to apply the derivative relationship to the data near the second dip in the cross section.[14] As the sign of the slope of the cross section changes, there is a sign change in the polarization, suggesting that the reaction mechanism may involve a simple exchange and that it is likely to be peripheral.

ACKNOWLEDGMENTS

We are indebted to R. Daly and W. Haberichter for their help with the MWPC system and R. Klem for the design of beam line 22B. We wish to thank H. Desportes for the design of the superconducting target magnet and Dr. S. T. Wang for assistance with this magnet. We also thank O. Fletcher, T. Kasprzyk, E. Millar, F. Onesto, and A. Rask for their help in setting up and running the experiment. We benefited from useful discussions with Dr. A. Beretvas and Dr. H. Spinka. Finally, the experiment would not have been possible without the excellent support of the ZGS operations staff. This work was supported by the U. S. Department of Energy.

*Present address: Bell Telephone Laboratories, Holmdel, New Jersey.

†Present address: LeMoyne College, Syracuse, New York.

‡Present address: Fermi National Accelerator Laboratory, Batavia, Illinois.

§Present address: General Electric Company, Milwaukee, Wisconsin.

||Present address: Bell Telephone Laboratories, Holmdel, New Jersey.

¶Present address: Purdue University, Lafayette, Indiana.

[1]For instance, see E. L. Berger and G. Fox, Nucl. Phys. B26, 1 (1971).

[2]G. Charpak, D. Rahm, and H. Steiner, Nucl. Instrum. Methods 80, 13 (1970); R. Bouclier, G. Charpak, Z. Dimcovski, G. Fischer, F. Sauli, G. Coignet, and G. Flugge, *ibid.* 88, 149 (1970).

[3]M. Fellinger *et al.*, Phys. Rev. Lett. 23, 600 (1969); Phys. Rev. 20, 1777 (1970).

[4]Manufactured by Edwards High Vacuum, Ltd., U. K., Model 18B4A.

[5]W. deBoer, J. Low Temp. Phys. 22, 85 (1976).

[6]J. J. Hill and D. A. Hill, Nucl. Instrum. Methods 116, 269 (1974).

[7]R. Esterling *et al.*, Phys. Rev. Lett. 21, 1410 (1968).

[8]J. Scheid *et al.*, Phys. Rev. D 8, 1263 (1973).

[9]M. Borghini *et al.*, Phys. Lett. 31B, 405 (1970); 36B, 493 (1971).

[10]D. M. Perkins, *Introduction to High Energy Physics* (Addison-Wesley, Reading, Mass., 1972).

[11]I. P. Auer *et al.*, Phys. Rev. Lett. 37, 83 (1976).

[12]I. P. Auer *et al.*, Phys. Lett. B113, 279 (1976).

[13]A. Yokosawa, BNL Report No. 20415, 1974 (unpub-

lished).
[14]F. Halzen, M. Olsson, and A. Yokosawa, Phys. Lett. B113, 269 (1976).
[15]S. W. Kormanyos *et al.*, Phys. Rev. 164, 1861 (1967).
[16]E. W. Hoffman *et al.*, Phys. Rev. Lett. 35, 138 (1975).
[17]R. J. Ott *et al.*, Phys. Lett. 42B, 133 (1972).
[18]R. Crittenden *et al.*, Phys. Rev. D 1, 3050 (1970).
[19]C. T. Coffin *et al.*, Phys. Rev. 159, 1169 (1967).
[20]G. Burleson *et al.*, Phys. Rev. Lett. 26, 338 (1971).
[21]D. Hill *et al.*, Phys. Rev. Lett. 27, 1241 (1971).
[22]H. Aoi *et al.*, Nucl. Phys. B64, 45 (1973).
[23]R. Birsa *et al.*, Nucl. Phys. B117, 77 (1976); B122, 397 (1977).